INORGANIC CHEMISTRY FRONTIERS

RESEARCH ARTICLE

View Article Online
View Journal | View Issue

Cite this: *Inorg. Chem. Front.*, 2026, **13**, 3186

Cycle contraction and symmetrisation in redox-active ligands: from alloxazine to isoimidazolonequinoxaline derivatives and their electrochemical and coordination studies

Jaison Casas,[a] Shaban Raja Muhammad,[a] David Pianca,[b] Nolwenn Le Breton,[b] Sylvie Choua,[b] Nathalie Kyritsakas,[c] Christophe Gourlaouen,[a] Abdelaziz Jouaiti[a] and Sylvie Ferlay *[a]

The formation of two parent divergent ligands derived from 1,4-bis(pyrid-3-yl)benzene is reported. The synthetic route involves condensation of alloxan with a dibromodiamine precursor, followed by benzylation, leading, after the Suzuki–Miyaura cross-coupling reaction, to the formation of two ligands: **L1**, bearing the well-known pteridine-dione moiety, and **L2**, in which ring contraction and symmetrisation occur, resulting in an imidazopyrazinone core. The synthesis of **L1** and **L2**, along with their characterization in solution and in the solid state, is reported. Electrochemical studies of **L1** and **L2** solutions revealed analogous two-electron reduction processes, with the first reduction step leading to radical species, as confirmed by EPR spectroelectrochemistry. For **L1**, the first and second reductions occur at E_{Red1} = −0,80 V and E_{Red2} = −1.35 V *vs.* Ag/AgCl, in agreement with the values reported for other pteridine-dione species, whereas **L2** displays more negative reduction potentials, shifted by approximately 0.7 V. These observations were confirmed by DFT calculations. The coordination abilities of **L1** and **L2** were investigated. Single-crystal X-ray diffraction (SCXRD) revealed the formation of a pillared 3D compound, **L2-Zn**, obtained by mixing **L2**, 4,4′-biphenyldicarboxylic acid (H_2bpdc) and a Zn^{2+} salt under solvothermal conditions. A series of powdered isostructural **L2-M** compounds (M = Zn, Ni, Co) was synthesized and characterized by powder X-ray diffraction (PXRD). Under the same conditions, using **L1** instead of **L2** led to the formation of poorly diffracting crystals, which nevertheless exhibited a three-dimensional pillared architecture. A complete series of powdered isostructural **L1-M** compounds (M = Co, Ni, Cu and Zn) was evidenced. The solid-state electrochemical behavior of the **L2-M** analogues (M = Zn and Co) was preliminarily investigated, revealing ligand-based reduction processes occurring within the three-dimensional pillared structure for both **L2-Zn** and **L2-Co**.

Received 22nd December 2025,
Accepted 27th January 2026

DOI: 10.1039/d5qi02572a

rsc.li/frontiers-inorganic

Introduction

Redox-active MOFs (RAMOFs),[1–3] a subclass of Metal Organic Frameworks (MOFs),[4–6] molecular crystalline materials, have received considerable attention due to their wide range of potential applications, including gas separation and purification, (electrochemical) sensing, photochromism, (photo)catalysis, electronic conductivity, magnetism, and energy storage devices such as rechargeable batteries and supercapacitors.[7] The specific feature of RAMOFs lies in their ability to finely tune physical properties through electron exchange processes, making them interesting multifunctional materials,[7] for example by improving charge transport within the network and enhancing the electrochemical response, as observed in electrochromic materials.[8] Different methodologies can be applied for the formation of RAMOFs, comprising the use of metal centers with different valence states,[2] the utilization of redox-active ligands,[9] the incorporation of organic redox-active guests, or combinations of these approaches. In RAMOFs, redox-active ligands serve as electron donors or acceptors and participate in oxidation–reduction processes. Integrating redox-active species into MOFs facilitates charge delocalization throughout the three-dimensional coordination network, a key factor for effective charge transport.

Among the various redox-active species used as ligands or guests for the formation of RAMOFs, one can cite tetrathiaful-

[a]*Université de Strasbourg, CNRS, CMC UMR 7140, F-67000 Strasbourg, France. E-mail: ferlay@unistra.fr*
[b]*Institut de Chimie, UMR CNRS 7177, Université de Strasbourg, Institut Le Bel, Strasbourg 67000, France*
[c]*Service de radiocristallographie de la Fédération de Chimie Le Bel-UAR 2042, Université de Strasbourg and CNRS, F-67000 Strasbourg, France*

valene (TTF),[10,11] anthraquinone (AQ),[12] tetracyanoquinodimethane (TCNQ),[13] naphthalene diimide (NDI),[14] perylene diimide (PDI),[15] triphenylene (TP),[16] pyrene, methyl viologen (MV^{2+}),[17] tetraphenylethylene (TPE),[18] porphyrin (Por),[19,20] 2,2,6,6-tetramethylpiperidin *N*-oxyl radical (TEMPO)[21] or perchlorotriphenylmethyl radical (PTM).[22,23] These compounds offer several advantages including their easy chemical functionalization, chemical and electrochemical stability and relatively low cost production, making them suitable for their implementation in different types of devices: electronic or energy storage, for example.

More recently, a new class of redox-active compounds, alloxazine, isomers of *iso*alloxazine related to flavins,[24] has emerged as promising materials to be used in energy storage devices.[25,26] They belong to a significant class of biomolecules characterized by three distinct protonation and redox states, including an accessible intermediate radical state. We recently reported a groundbreaking redox-active divergent ligand derived from *iso*alloxazine, together with the formation of related coordination polymers[27] and porous materials[28,29] derived from pillared MOFs,[30,31] that exhibit redox activity.

In the context of developing stable redox-active compounds for electrochemical energy storage,[32] we report here two redox-active ligands based on 1,4-bis(pyrid-3-yl)benzene that are suitable for the construction of pillared metal–organic frameworks (MOFs):[28,29] **L1** is derived from the pteridine-dione core (pyrimidine-2,4-dione, 6 membered ring) and **L2** is derived from the imidazopyrazinone core (imidazolidin-2-one, 5 membered ring). In order to increase the solubility and stability of such compounds, particularly in aqueous solution, benzyl moieties were introduced on the core for **L1** and **L2** (Scheme 1). To the best of our knowledge, ligands based on isoimidazolonequinoxaline and their electrochemical properties have not been previously reported. The synthesis, characterization, electrochemical behaviours and coordination abilities of ligands **L1** and **L2** are reported. Herein, we present a comparative investigation of the electrochemical and coordination properties of two closely related redox-active ligands, one of which has undergone ring contraction and symmetrisation.

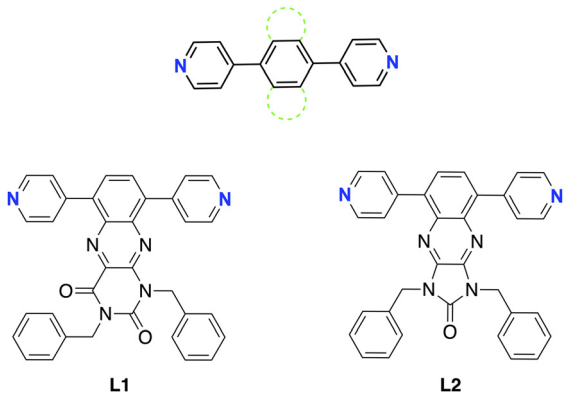

Scheme 1 The investigated ligands **L1** and **L2**.

Results and discussion

Synthesis and formation of L1 and L2

L1 and **L2** were synthesized in a four-step sequence, adapted from the methodology recently reported (Scheme 2).[27] The dibromodiamine precursor **1** was first prepared by reduction of a dibrominated thiadiazole derivative; then **1** was condensed with alloxan under acidic conditions, leading to the formation of **2**, a dibromo-alloxazine. **2** was then appended on the nitrogen atoms of the alloxan moiety by the benzyl group, and during this process, performed in the presence of oxygen, two dibromo compounds were obtained: **3** (29% yield), presenting an alloxazine core and the symmetrical **4**, displaying an imidazoquinoxalinone 5-membered ring (56% yield), evidencing a ring reduction during this step. It is noteworthy that compound **3** can be isolated in higher yield under anaerobic conditions. On both **3** and **4**, the pyridyl moiety was then introduced *via* a Suzuki–Miyaura cross-coupling, affording **L1** and **L2** in 39% and 37% yield, respectively (see the Experimental part).

During step 3 of the reaction, the nucleophilic substitution with bromobenzyl under aerobic conditions, a ring reduction to imidazo[4,5-*b*]quinoxaline and thus symmetrisation of the moiety occurred. Similar results were observed under anaerobic conditions; however, the yields were lower. This phenomenon was already described in the literature, while performing the alkylation of the alloxazine disodium salt[33] or the conversion of 1,3-dialkyl-7-azapteridines into 1,3-dialkyl-6-azapurines.[34] The

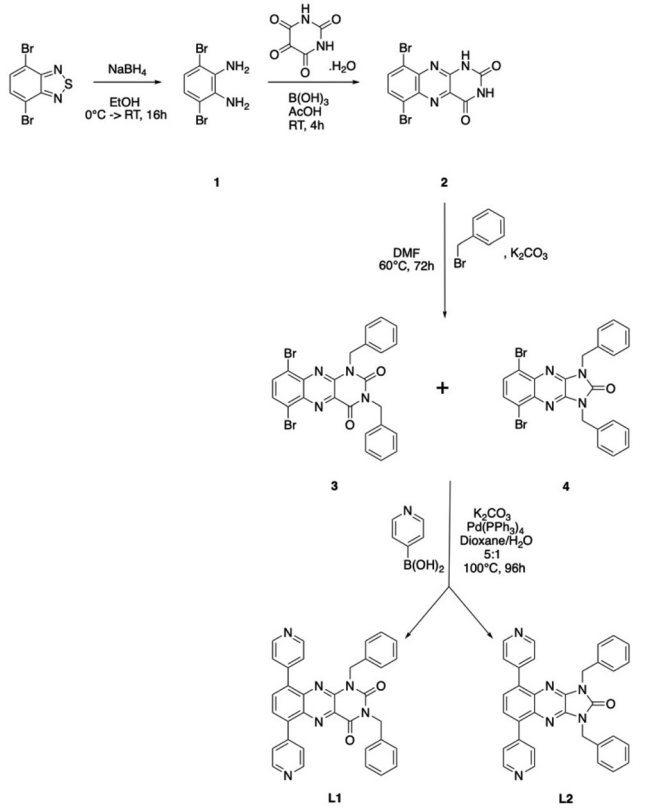

Scheme 2 Synthetic pathway for the formation of **L1** and **L2**.

literature reports a partial mechanism[35–38] of ring contraction under basic conditions, proceeding through ring opening and decarboxylation to form a quinoxalinone intermediate.[39] In addition, the photochemical reactivity of imidazo[4,5-*b*]quinoxaline derivatives has been reported only very recently[39] and to the best of our knowledge, the redox properties of such species have not been exploited yet; only those of pyrido-[1′,2′:1,2]imidazo[4,5-*b*]quinoxaline have been reported.[40]

As a consequence of this phenomenon, **L2** ligand (Fig. 1) displays a symmetrical redox-active core (imidazopyrazinone), whereas **L1** contains a redox-active pteridine-dione unsymmetrical core. **L1** and **L2** have been characterized thoroughly in solution (see the Experimental section), and optical and electrochemical properties are reported here.

Optical characterization of L1 and L2. Both compounds are yellow-coloured solids emissive compounds, as confirmed by their absorption behaviour. Nevertheless, the properties have been investigated in CH_2Cl_2 solution. For **L1**, two distinct absorption bands are observed at 351 nm (ε = 17 450 L mol^{-1} cm^{-1}) and 393 nm (ε = 9650 L mol^{-1} cm^{-1}), which can be assigned to π–π* and n–π* transitions, respectively. **L2** exhibits two closely spaced absorption bands at 338 nm (ε = 24 920 L mol^{-1} cm^{-1}) and 354 nm (ε = 24 360 L mol^{-1} cm^{-1}).

Both compounds are emissive in solution (λexc = 320 nm for **L1** and λexc = 349 nm for **L2**) and the emission spectrum of **L1** displays two maxima at 382 nm and 457 nm, whereas **L2** exhibits only a single emission peak at 382 nm (Fig. S1).

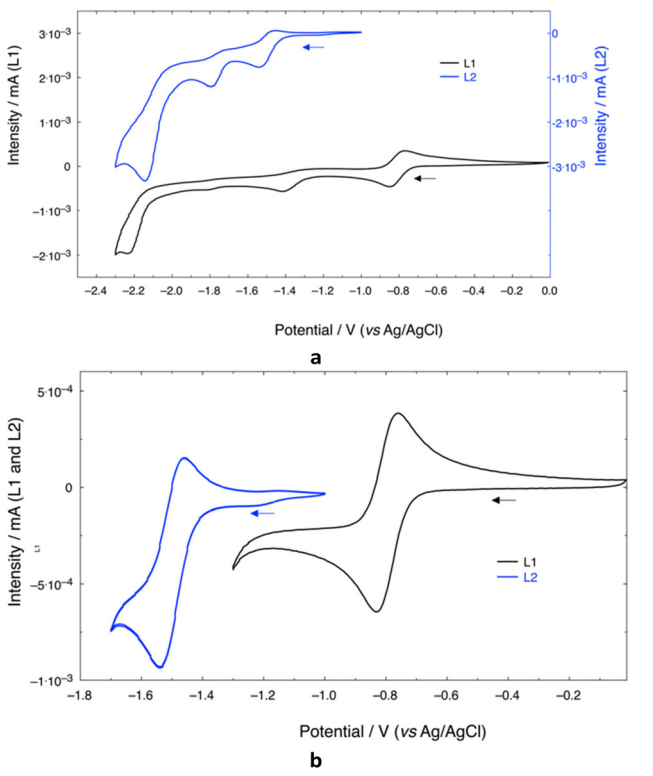

Fig. 1 For **L1** and **L2**: (a) full voltammogram of **L1** and **L2**, see the appropriate scale on the Y-axis; (b) zoom on the reversible redox event of **L1** and **L2**; measurements were conducted in 1 mM solutions of ligand in DMF and containing 0.1 M $TBABF_4$ as the supporting electrolyte. WE: glassy carbon disk. RE: Ag/AgCl. CE: platinum wire. Scan rate: 20 mV s^{-1}.

Redox behaviour of L1 and L2. The redox properties of **L1** and **L2** were studied by electrochemical methods in solution. Cyclic voltammetry (CV) using a glassy carbon working electrode in DMF solutions with tetrabutylammonium tetrafluoroborate ($TBABF_4$ 0.1 M) as the supporting electrolyte and an Ag/AgCl reference electrode was performed (see Fig. 1). For **L1**, the first reduction wave appears at E_{Red1} = −0.80 V and E_{Red2} = −1.35 V *vs.* Ag/AgCl. While the first reduction appears reversible and can be attributed to the formation of the radical species associated with a proton transfer, the second is much less reversible and can be attributed to the formation of the doubly reduced much more unstable species, as already observed for the parent methylated compound, and more generally[27] flavin mononucleotide.[41,42] **L2** exhibits a CV profile similar to the one observed for **L1**; however, its first reduction occurs at a much lower potential (E_{Red1} = −1.50 V, shifted by 0.70 V *vs.* AgCl). This feature is consistent with the formation of a radical species, reflecting a more challenging but still reversible reduction. The sharp and symmetric shape of the first couple, along with the nearly identical peak currents for reduction, confirms the rapid electron-transfer kinetics of this redox pair.

Through this study, it appeared that **L2** is less oxidizing, with a significant shift towards low potentials, in the ground state. This can be explained by the missing carbonyl group on the imidazolidin-2-one 5 membered ring. The first reduction potential value of **L2** is close to those of the quinoxaline radical anion bearing an electron-withdrawing substituent.[43,44] Although the π-system of **L2** is slightly more extended, the presence of two trivalent nitrogen atoms acting as π-donors, together with the absence of the carbonyl group on its five-membered ring compared to **L1**, lowers the reduction potential. This effect likely arises from increased electron density within the aromatic core (*vide infra*). Furthermore, this behavior is associated with charge delocalization along the rings of **L1** and **L2**, as supported by the DFT calculations presented here.

As a conclusion, **L1** [45] and **L2** exhibit distinct two-electron redox profiles and the proposed redox states are depicted in Scheme S1 for **L2** and admitted for **L1**.

Electrochemical generation of radicals and coupled EPR spectroscopy studies of L1 and L2. Electrochemical reduction combined with electron paramagnetic resonance (EPR) spectroscopy was subsequently employed to generate intermediate radical anions at the redox potentials previously determined by cyclic voltammetry (CV). Cathodic reduction of **L1** and **L2** in DMF produced well-resolved EPR spectra (see Fig. 2 and Scheme S2 for labelling the atoms on **L2**). The pattern for **L2** arises from hyperfine coupling (hfc) of the unpaired electron with two sets of two nuclei (^{14}N) and two sets of two protons (^{1}H). The largest hyperfine coupling constants (0.21 mT) and (0.15 mT) are attributed to the nitrogen atoms on quinoxaline (N4 and N7) and on imidazolone (N1 and N3) rings respectively, while the coupling constant of similar magnitude

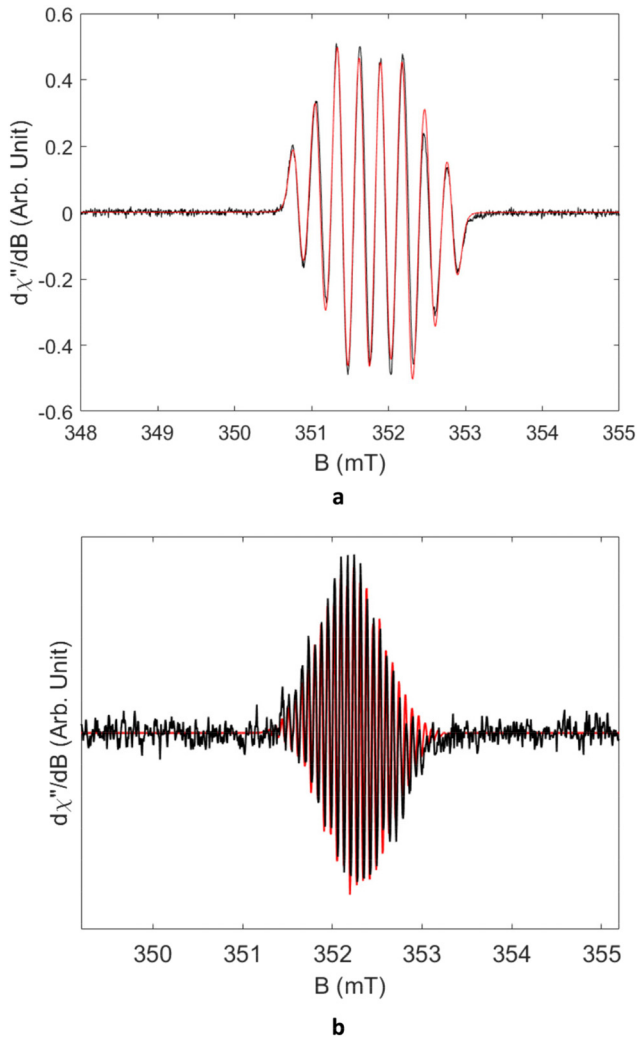

Fig. 2 For **L1** (a) and **L2** (b): X-band EPR spectrum of 1 mM electrochemically generated one-electron reduced species. Solid black line, experimental; red line, simulation using parameters specified in the text (a) power = 2 mW; modulation frequency = 100 kHz, modulation 0.3 G, number of scans = 10 (b) power = 5 mW; modulation frequency = 100 kHz, modulation 1 G, number of scans = 10.

(0.13 mT) corresponds to protons H5 and H6. Moreover, the significantly smaller couplings of 0.07 mT associated with the *ortho* substituted pyridine proton provide complementary information regarding the extended electron delocalization and overall spin-density distribution within the anionic species. In contrast, the EPR pattern of **L1** displays two distinct sets of one nitrogen nucleus (^{14}N) hfc (N4 and N7 0.56 and 0.36 mT respectively) and one set of one proton (^{1}H) (H5 and H6, 0.27 mT) as previously observed,[27] indicating a lower degree of delocalization of the unpaired electron.

These data confirm the hypothetic electron exchange pathways proposed for **L2** in Scheme S1, with the radical fully delocalized on the quinoxaline and imidazolone rings.

DFT calculations. Based on the cyclic voltammetry of **L1**, the structural fusion of the quinoxaline core with imidazolone extends the aromatic π-conjugation, thereby enhancing the stability of the radical anion with a less negative E_{Red1} compared to that of quinoxaline. Density functional theory (DFT) calculations were employed to compare **L1** and **L2**.

The lowest unoccupied molecular orbital (LUMO) of **L2** (and **L1**) and the singly occupied molecular orbital (SOMO) of **L2**$^{\bullet-}$ (and **L1**$^{\bullet-}$) depicted in Fig. S2 are almost identical. This indicates that the added electron occupies the LUMO of the initially oxidized ligand, effectively converting it into the SOMO upon reduction.

The **L1** and **L2** scaffolds are planar and their SOMO is of π-type. The two nitrogen atoms of the imidazolone core on **L2** lie in the nodal plane of the quinoxaline π-electron system facilitating the extension of conjugation and suggesting a hyperfine coupling mechanism based on spin polarization. The condensed Mulliken spin densities of both **L2**$^{\bullet-}$ and **L1**$^{\bullet-}$ indicate that the added electron is fully delocalized over **L2**$^{\bullet-}$ with a higher spin density concentrated on the imidazolone core (Fig. 3). This increase in electron density within the fully aromatic core raises the reduction potential, thereby making reduction more difficult. The computed HOMO–LUMO energy gaps of the two ligands follow the same trend (3.652 eV for **L1** *vs.* 4.117 eV for **L2**). This confirms the Electrochemical and EPR data.

Formation of pillared MOFs with L1 and L2. While the coordination behavior of ligands through the pteridine-dione moiety of alloxazine derivatives has been widely studied,[46,47] the present work examines the coordination potential of **L1** and **L2** *via* the pyridine donor sites appended on the alloxazine core, using a three-component strategy, in order to build "pillared MOFs",[30,31] under solvothermal conditions as presented in Scheme 3.

Solvothermal reactions were conducted using **L2** and H_2**bpdc** (4,4′-biphenyldicarboxylic acid, H_2**bpdc**) with three divalent metal salts. Reactions involving Ni^{2+} and Zn^{2+} salts led to the formation of single crystals which were analysed by single crystal X-ray diffraction (see Table S2). Both compounds crystallise in the monoclinic *C*2/*c* space group, are isometric, and present the formula $2((C_{14}H_8O_4)_2C_{33}H_{24}N_6OM_2)$, nC_3H_7NO [+solvent] (M = Co or Zn and n = 1 for M = Ni and n = 2 for M = Zn) or more generally $(bpdc)_2M_2$**L2**·nDMF (**L2-M**). The descrip-

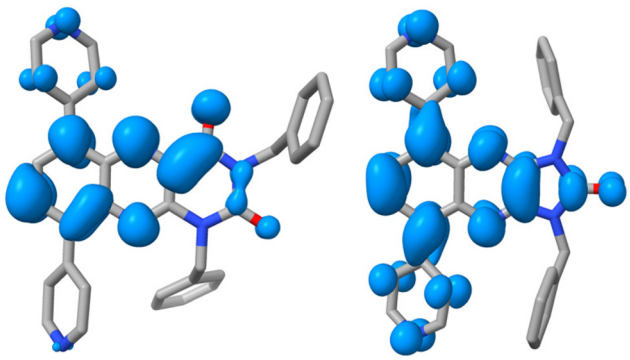

Fig. 3 Spin density maps of **L1**$^{\bullet-}$ (left) and **L2**$^{\bullet-}$ (right). Hydrogen atoms are omitted for clarity.

Scheme 3 Synthetic pathways for the formation of **L1-M** (M = Co, Ni, Cu and Zn) and **L2-M** (M = Co, Ni and Zn).

tion of the structure will be performed for **L2-Zn**, since for **L2-Ni** the structure was poorly refined, but both compounds are isostructural, as seen from the crystallographic data (Table S2). The asymmetric unit is composed of two $bpdc^{2-}$ ligands, one ligand **L2**, two M^{2+} cations and one (M = Ni) or 2 (M = Zn) and free DMF molecule (see Fig. S4). In **L2-Zn**, disorder is observed both on the pyridyl rings and on the benzyl moieties appended to **L2**. As already observed,[28,29] the connectivity in **L2-Zn** can be described as the formation of Zn_2 paddlewheels (short Zn–Zn distance of 2.9186(5) Å), (Table S3), where the Zn^{2+} cations adopt a distorted square pyramidal geometrical environment. These Zn_2 paddlewheels (see Fig. S3) are the corner square connecting units surrounded by four disordered **pbdc**$^{2-}$ ligands, ensuring the 1 : 1 metal-to-ligand stoichiometric ratio: this results in the formation of a 2D lozenge-shaped lattice (close to a distorted square grid), with sides measuring 15.170 (8) Å and an angle of 77.63° (Fig. 4a). These 2D "grids" stack into layers interconnected by **L2** ligands, resulting in a pillared 3D network with a metal : **pbdc** : **L2** stochiometric ratio of 2 : 2 : 1, as shown in Fig. 4b. Refined DMF molecules are also present in the network. The crystal structure contains two interpenetrating 3D networks as shown in Fig. S3, leading to channels with a reduced diameter of *ca.* 8.5 Å. The two networks interact with each other through π–π stacking between the imidazolonequinoxaline (**L2**) cores and the phenyl groups from the **pbdc**$^{2-}$ ligands as shown in Fig. 4c.

For both compounds **L2-Zn** and **L2-Ni**, the squeeze command of Platon[48] was used for the structure refinement. The residual electron density (222 for **L2-Ni** or 81 for **L2-Zn**) was assigned to five (**L2-ZNi**) or two (**L2-Zn**) additional molecules of the *N*,*N*-dimethylformamide solvent per asymmetric unit, which could not be refined.

Attempts to obtain an isostructural compound of **L2-Ni** or **L2-Zn** were made using the same conditions and the Co^{2+} cation. A powdered compound was obtained (**L2-Co**) that was analysed using PXRD, as shown in Fig. S5. It evidenced the formation of a series of 3 isostructural polycrystalline compounds **L2-Ni**, **L2-Zn** and **L2-Co**.

Solvothermal reactions, under the same conditions but involving **L1**, H_2bpdc (4,4′-biphenyldicarboxylic acid, H_2bpdc) and metallic salts, were performed with three divalent metal salts. Poorly diffracting single crystals were obtained using a Co^{2+} salt, leading to a compound named **L1-Co**. The cell parameters could be estimated by SCXRD (see Table S4). Despite analysis of the single crystals at a synchrotron facility, only a preliminary structure could be obtained, which could not be completely solved. Preliminarily diffraction data showed that **L1-Co** adopts the same arrangement as observed in parent compounds, Fig. S4.[28,29] Pictures of the preliminarily solved structure are shown in the SI, revealing a strong disorder for **L1**. A series of 4 powdered isostructural compounds could thus be obtained starting from Co^{2+}, Ni^{2+}, Cu^{2+} or Zn^{2+} salts, as shown by the PXRD diagrams, leading to a whole series of polycrystalline isostructural compounds **L1-M** (M = Co, Ni, Cu and Zn) (Fig. S6).

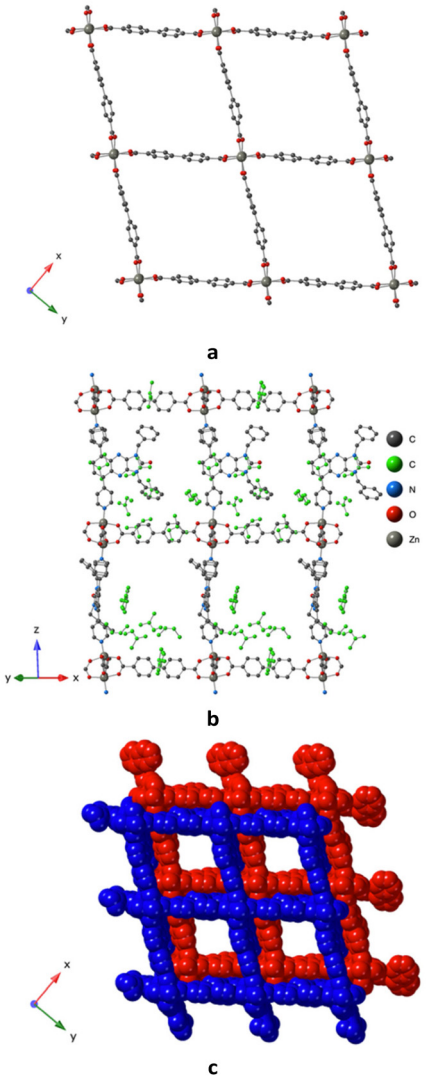

Fig. 4 The X-ray crystal structures of **L2-Zn**, representation showing: (a) the 2D grid formed by the dicarboxylate ligands; (b) the connectivity of the 2D layers with the pillared ligands thus forming 3D compounds with refined DMF molecules inside the cavities; (c) the interpenetration of two 3D compounds, thus forming the resulting crystal structure. H atoms were omitted for clarity. Disordered pyridyl species are not represented.

For **L2-M** (M = Zn, Ni and Co) and **L1-M** (M = Zn, Ni, Co and Cu), the TGA traces reveal a stability depending on the nature of the metal: the decomposition temperature around 400 °C for **L1-M** (M = Co, Ni and Zn) and **L2-Co** and **L2-Zn**, 350 °C for **L1-Cu** and 320 °C for **L2-Ni** (Fig. S6). The measurements revealed significant solvent losses, making it impossible to accurately determine the exact number of solvent molecules present in each sample (*i.e.*, adsorbed H_2O and DMF).

For **L1-M** (M = Co and Zn), after careful activation (see the Experimental section), N_2 adsorption measurements were performed. The compounds indicate a type I sorption profile (see Fig. S7), and using the BJH model,[49] the highest surface areas of 698 $m^2\ g^{-1}$ and 641 $m^2\ g^{-1}$ were determined, with the pore size estimated to be 12 and 14 Å for **L1-Co** and **L1-Zn** respectively.

For the **L2-M** compounds, an insufficient amount of material was available to carry out the adsorption measurements.

Electrochemical studies of L2-Zn and L2-Co in the solid state. Solid-state electrochemical investigations of **L2-Zn** and **L2-Co** were performed in order to track the formation of the radical species from **L2** when embedded in a **L2-M** MOF. Thin films of **L2-Zn** and **L2-Co** were obtained by drop-casting crystals of **L2-Zn** on a glassy carbon electrode immersed in DMF (see the Experimental section). The compound presents a chemically reversible reduction peak at *ca.* −1.4 V (*vs.* Ag/AgCl) (Fig. 5). However, the process is electrochemically irreversible due to slow kinetics and the solid–liquid interface. Due to the slightly different reduction potential compared to the ligand **L2**, the observed reduction cannot be attributed to the metal center. This is consistent with ligand-centered reduction leading to the formation of a radical anionic species $\mathbf{L2}^{\bullet-}$. This illustrates the potential of the family of compounds (**L2**) to be used in RAMOFs.

Unfortunately, due to a small amount of reduced compounds in the solid state (films), further characterization (PXRD, gas sorption or TGA) of the reduced MOF species could not be performed.

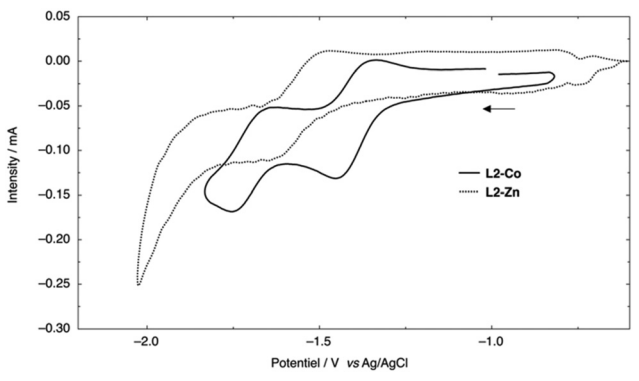

Fig. 5 Cyclic voltammograms of the first reduction for films (i) of **L2-Co** and (ii) **L2-Zn** deposited in the sold state on the WE electrode with 0.1 M $TBABF_4$: working electrode = glassy carbon, reference electrode = Ag/AgCl, counter electrode = Pt. Scan rate: 40 mV s^{-1}.

Experimental

Synthetic procedures

L1 and **L2** have been obtained using a synthetic pathway already reported by us (see Scheme 2), and **1** and **2** intermediates have been already described.[27]

Synthesis of 3 and 4. **2** (0.25 g, 0.67 mmol) and K_2CO_3 (0.4 g, 2.9 mmol) were dissolved in DMF (15 mL) under air. The mixture was heated at 70 °C for 1 h, and then K_2CO_3 (0.4 g, 2.9 mmol) and benzyl bromide (0.5 g, 2.9 mmol) were added. The resulting mixture was stirred at 70 °C for 72 h. After cooling, the reaction mixture was evaporated to dryness. The resulting yellow solid was dissolved in dichloromethane and washed successively with water and saturated brine (2 × 50 mL). The organic layer was dried with anhydrous $MgSO_4$ and the solvent was evaporated to afford an orange solid. The crude product was purified by column chromatography (SiO_2) to yield **3** and **4** (eluant, CH_2Cl_2/petroleum ether 1 : 1).

3: yellow solid in 29% yield.

Compound **3** could be synthesized under the same precedent conditions with a higher yield (up to 90%) by carrying out the reaction under argon.

^{1}H NMR ($CDCl_3$, 500 MHz, 25 °C) δ ppm: 8.03 (d, J = 8.1 Hz, 1H), 7.90 (d, J = 8.1 Hz, 1H), 7.80–7.74 (m, 2H), 7.64–7.58 (m, 2H), 7.36–7.27 (m, 6H), 5.68 (s, 2H), 5.37 (s, 2H).

^{13}C NMR ($CDCl_3$, 126 MHz, 25 °C) δ ppm: 136.81, 132.51, 129.84, 129.60, 128.60, 128.57, 128.24, 128.15, 46.33, 46.01.

ESI-MS: m/z $[M + H]^+$ calcd for $C_{24}H_{17}N_4O_4Br_2$ $[M + H]^+$ 572.9532; found 572.9528.

4: white solid, 0.2 g in 56% yield.

^{1}H NMR ($CDCl_3$, 500 MHz, 25 °C) δ ppm:.7.75 (s, 2H), 7.69 (m, 4H), 7.34 (m, 6H), 5.24 (s, 4H).

^{13}C NMR ($CDCl_3$, 126 MHz, 25 °C) δ ppm: 153.8, 140.3, 137.8, 135.2, 130.5, 129.6, 128.8, 128.4, 121.9, 50.9.

ESI-MS: m/z $[M + H]^+$ calcd for $C_{23}H_{17}N_4O_4Br_2$ $[M + H]^+$ 522.9763; found 522.9759.

Synthesis of L1. **3** (0.602 g, 1.09 mmol) was suspended in a mixture of 1,4-dioxane/water (5 : 1, 60 mL) together with 4-pyridylboronic acid (0.408 g, 3.31 mmol) and K_2CO_3 (0.600 g, 4.34 mmol). The flask was placed under argon, and $Pd(PPh_3)_4$ (68 mg, 0.059 mmol, ∼5 mol%) was added, resulting in a homogeneous orange solution. The reaction mixture was stirred at 100 °C for 4 days under an inert atmosphere. After cooling to room temperature, the solvent was evaporated under reduced pressure. The resulting solid was dissolved in CH_2Cl_2 (50 mL) and washed with brine (3 × 50 mL). The organic phase was then concentrated and the crude product was purified by silica gel column chromatography (CH_2Cl_2/CH_3OH 99.5 : 0.5) to afford **L1** as a yellow solid (0.232 g, 0.42 mmol, 38.8%).

^{1}H NMR ($CDCl_3$, 500 MHz, 25 °C) δ ppm: 8.92–8.76 (m, 2H), 8.70–8.60 (m, 2H), 8.15 (d, J = 7.9 Hz, 1H), 7.93 (d, J = 7.4 Hz, 1H), 7.84 (d, J = 7.5 Hz, 1H), 7.78 (d, J = 7.9 Hz, 1H), 7.51–7.33 (m, 4H), 7.26–7.17 (m, 3H), 7.07 (td, J = 8.9, 4.6 Hz, 3H), 6.98 (d, J = 7.2 Hz, 2H), 5.37 (s, 2H), 5.27 (s, 2H).

^{13}C NMR ($CDCl_3$, 126 MHz, 25 °C) δ ppm: 158.84, 150.70, 150.66, 150.47, 149.42, 149.17, 144.53, 141.40, 138.84, 138.69, 138.05, 137.82, 136.26, 136.12, 135.77, 133.86, 133.56, 132.93, 132.16, 132.08, 129.55, 129.37, 129.07, 128.59, 128.45, 128.35, 128.06, 127.76, 123.13, 45.89.

IR bands (cm^{-1}): 1722 (medium), 1677 (strong), 1585 (weak), 1555 (strong), 1496 (medium), 1472 (medium), 1397 (strong), 1327 (medium), 1280 (medium), 1239 (strong), 1224 (strong), 1075 (weak), 1025 (medium), 802 (medium), 747 (medium), 700 (strong), 632 (medium), 606 (medium), 554 (weak), 508 (strong), 453 (weak).

MS (ESI-MS): *m*/*z* calculated for $C_{34}H_{24}N_6O_2$, 548.20; found, 549.20 $[M + H]^+$.

UV: ε (351 nm) = 17 450 L mol^{-1} cm^{-1}; ε (393 nm) = 9650 L mol^{-1} cm^{-1} (see Fig. S1).

Elemental analysis: Anal. calc. for $C_{37}H_{30}N_6O_3$ ($C_{34}H_{24}N_6O_2{\cdot}CH_3COCH_3$), N, 13.85%; C, 73.25%; H, 4.98%; found, N, 13.85%, C, 73.25%; H, 4.98%.

Synthesis of L2. **4** (0.566 g, 1.08 mmol), 4-pyridylboronic acid (0.511 g, 4.15 mmol), and K_2CO_3 (0.898 g, 6.50 mmol) were suspended in a mixture of 1,4-dioxane/water (5 : 1, 60 mL). The flask was placed under argon and $Pd(PPh_3)_4$ (62.4 mg, 0.054 mmol, 5 mol%) was added. The dissolution of all components was observed at 65 °C, resulting in a clear orange-red solution. The reaction mixture was stirred at 100 °C for 4 days. At the end of the reaction, the dark rust-colored mixture was cooled to room temperature and extracted with CH_2Cl_2 (3 × 50 mL), and the organic layers were washed with brine (3 × 50 mL). The organic phase evaporated under reduced pressure. The crude product was purified by column chromatography (silica gel, CH_2Cl_2/methanol 99.5 : 0.5) to afford **L2** as a yellow solid (0.205 g, 0.40 mmol, 37.4%).

^{1}H NMR ($CDCl_3$, 300 MHz, 25 °C) δ ppm: 8.75 (d, J = 5.7 Hz, 4H), 7.68 (s, 2H), 7.54 (d, J = 5.7 Hz, 4H), 7.43 (dd, J = 9.6, 1.8 Hz, 4H), 7.35–7.30 (m, 6H), 5.093 (s, 4H).

IR bands (cm^{-1}): 3031 (weak), 1723 (medium), 1672 (strong), 1590 (medium), 1560 (strong), 1495 (weak), 1396 (strong), 1327 (medium), 1280 (medium), 1239 (strong), 1224 (strong), 1075 (weak), 1026 (weak), 811 (strong), 746 (medium), 690 (strong), 626 (medium), 509 (strong), 488 (medium).

Elemental analysis: Anal. calc. for $C_{33.2}H_{24.8}N_6O_{1.2}$ ($C_{33}H_{24}N_6O{\cdot}0.2MeOH$), N, 15.95%, C, 75.66%; H, 4.74%; found, N, 15.93%; C, 75.53%; H, 4.64%.

UV: ε (338 nm) = 24 920 L$mol^{-1}cm^{-1}$; ε (354 nm) = 24 360 L mol^{-1} cm^{-1} (see Fig. S1).

MS (ESI-MS): *m*/*z* calculated for $C_{33}H_{24}N_6O$, 520.60; found, 521.21 $[M + H]^+$.

Synthesis of L2-Ni. **L2** (26 mg, 0.05 mmol, 1 eq.), Ni(II)nitrate hexahydrate (29 mg, 0.1 mmol, 2 eq.), and **H_2pbdc** (22 mg, 0.1 mmol, 2 eq.) in 6 mL DMF were placed inside a sealed glass vessel. The vessel was heated at 120 °C for 110 hours and after that dark green plate-like single-crystals were formed in 75% yield, which were suitable for SXRD analysis.

Anal. calc. for $(C_{14}H_8O_2)_2(C_{33}H_{24}N_6O)Ni_2{\cdot}(C_3H_7NO)8(H_2O)$: N, 7.71%, C, 60.45%; H, 4.99%; found, N, 7.62%; C, 62.56%; H, 4.93%.

Synthesis of L2-Zn. The same procedure was followed by replacing Ni(II)nitrate hexahydrate by Zn(II)nitrate hexahydrate (30 mg, 0.1 mmol, 2 eq.). Yield 46%.

Anal. calc. for $(C_{14}H_8O_2)_2(C_{33}H_{24}N_6O)Zn_2{\cdot}4(C_3H_7NO)$ 3 (H_2O): N, 9.90%, C, 61.99%; H, 5.27%; found, N, 9.85%; C, 62.43%; H, 5.15%.

Synthesis of L2-Co. The same procedure was followed by replacing Ni(II)nitrate hexahydrate by Co(II)nitrate hexahydrate (30 mg, 0.1 mmol, 2 eq.). Yield 68%.

Anal. calc. for $(C_{14}H_8O_2)_2(C_{33}H_{24}N_6O)Co_2{\cdot}(C_3H_7NO)$ 6(H_2O): N, 7.93%, C, 62.19%; H, 4.81%; found, N, 7.86%; C, 62.48%; H, 4.85%.

Synthesis of L1-Co. The same procedure was followed by using Co(II)nitrate hexahydrate (30 mg, 0.1 mmol, 2 eq.) and **L1** (20 mg, 0.05 mmol, 1 eq.). Yield 45%.

Anal. calc. for $(C_{14}H_8O_2)_2(C_{34}H_{24}N_6O_2)Co_2{\cdot}6(C_3H_7NO)4$ (H_2O): N, 10.55%, C, 60.30%; H, 5.7%; found, N, 10.60%; C, 61.56%; H, 5.60%.

Synthesis of L1-Ni. The same procedure was followed by using Ni(II)nitrate hexahydrate (30 mg, 0.1 mmol, 2 eq.). Yield 66%.

Anal. calc. for $(C_{14}H_8O_2)_2(C_{34}H_{24}N_6O_2)Ni_2{\cdot}5(C_3H_7NO)$: N, 10.64%, C, 63.87%; H, 5.22%; found, N, 10.55%; C, 62.49%; H, 5.30%.

Synthesis of L1-Zn. The same procedure was followed by using Zn(II)nitrate hexahydrate (30 mg, 0.1 mmol, 2 eq.). Yield 70%.

Anal. calc. for $(C_{14}H_8O_2)_2(C_{34}H_{24}N_6O_2)Zn_2{\cdot}10(C_3H_7NO)4$ (H_2O): N, 11.80%, C, 58.19%; H, 6.26%; found, N, 11.72%; C, 60.26%; H, 6.24%.

Synthesis of L1-Cu. The same procedure was followed by using Cu(II)nitrate hexahydrate (30 mg, 0.1 mmol, 2 eq.). Yield 35%.

Anal. calc. for $(C_{14}H_8O_2)_2(C_{34}H_{24}N_6O_2)Cu_2{\cdot}6(C_3H_7NO)3$ (H_2O): N, 10.60%, C, 60.63%; H, 5.60%; found, N, 10.42%; C, 60.42%; H, 5.58%.

For the 4 compounds, IR (cm^{-1}) ν: 1659 (s), 1610 (m), 1093 (w), 826 (w), 771 (s), 680 (m), 661 (m), 468 (s).

Materials and methods

FT-IR spectra of the powdered microcrystalline samples were recorded on a PerkinElmer Spectrum Two FTIR-UATR in the wavenumber interval of 4000–400 cm^{-1}. Absorbance spectra were recorded on a PerkinElmer Lambda 650 spectrometer. Emission spectra were recorded on a PerkinElmer LS55 spectrophotometer. Low-pressure gas sorption measurements (N_2) were obtained on a Micromeritics ASAP 2020 analyser. Powdered microcrystalline samples were activated under dynamic vacuum at a temperature of 160 °C over 12 h. TGA measurements were performed on powdered microcrystalline compounds on a Pyris 6 TGA Lab System (PerkinElmer), using a N_2 flow of 20 mL min^{-1} and a heating rate of 4 °C min^{-1}.

Electrochemical procedure. The electrochemical measurements were carried out at RT (20 °C) in DMF containing 0.1 M $TBABF_4$ in a classical three-electrode cell. The working electrode was a 3 mm glassy carbon disk, the counter electrode

was a Pt wire, and an Ag(s)|AgCl(s) electrode was selected as a reference. The electrolyte was degassed by bubbling argon through the solution for at least 10 min, and the argon flow was kept over the solution during the measurements. The electrochemical cell was connected to a computerised multipurpose electrochemical device (BIOLOGIC potentiostat, model SP-150). Cyclic voltammetry experiments were performed at a scan rate varying from 20 mV s^{-1} to 100 mV s^{-1}. CVs that are presented are corrected for the ohmic drop.

L2-Co and **L2-Zn** have been investigated in the solid state: the deposition on the glassy carbon electrode was performed by suspending microcrystalline powder of **L2-Co** (or **L2-Zn**) in an EtOH solution, then the solution was drop-cast on the surface of the electrode and dried in air, in order to cover the entire glassy carbon disk.

EPR measurements. Continuous-wave EPR spectra were recorded on an EMX spectrometer (Bruker Biospin GmbH), equipped with a high sensitivity resonator (4119HS-W1, Bruker) operating at X-band. Spectra were recorded at room temperature. Computer simulations of the EPR spectra were performed with the help of easyspin software.[50] Radical anions were generated *in situ* by electrolysis in the EPR quartz tube. Electrolysis was performed at a controlled potential (applied on the first reduction potential) with a three-electrode configuration under argon using a platinum wire as the working electrode, a platinum wire as the auxiliary electrode and a silver wire as the pseudo reference electrode. A 10^{-3} M solution of **L1–L2** was prepared in DMF + $TBABF_4$ (0.1 M) as the supporting electrolyte and degassed under argon.

DFT calculations. Ground state electronic structures for **L1–L3** were computed using the Amsterdam Density Functional (ADF2024)[51] at the DFT level of theory (B3LYP functional)[52] including dispersion corrections (Grimme's gd3).[53] A standard triple-ζ Slater basis (TZP) set was used for all atoms.[54,55] The DMF solvent effect was introduced by the COSMO model.[56] All geometries were fully optimized and for open-shell unrestricted formalism was employed.

The ORCA package[57,58] was used to calculate EPR properties through a single point on ADF-optimized geometries using the B3LYP/G functional in combination with 6-31g* basis sets.

Crystallography

SCXRD. Intensity data were collected for **L2-Ni**, **L1-Co** and **L2-Zn**, using a 4-circle Bruker PHOTON III diffractometer equipped with two micro-sources IμS Mo and IμS Diamond Cu, along with an Oxford Cryosystem 800 for low temperature measurements. The cell parameters were determined using APEX3 software,[59] and the structures were solved using the program SHELXT-2014.[60] The refinement and all further calculations were carried out using SHELXL-2018.[61] Hydrogen atoms were included in calculated positions and treated as riding atoms using SHELXL default parameters. The non-H atoms were refined anisotropically, using weighted full-matrix least-squares on F^2. A semi-empirical absorption correction was applied using SADABS in APEX3.

CCDC for **L2-Zn**: 2515971.

The cif file of poorly refined **L2-Ni** and **L1-Co** is provided as an example in the SI.

PXRD. Diffractograms for the air-dried microcrystalline samples were recorded at room temperature (293(2) K), on a Bruker D8 diffractometer using monochromatic Cu-Kα radiation. A scanning range between 2° and 40° with a scan step size of 2° min^{-1} was used, and the sample holder was rotated at 15 rpm.

Conclusions

The formation of **L1** and **L2** demonstrates the feasibility of generating redox-active ligands derived from 1,4-bis(pyrid-3-yl) benzene. These ligands can be investigated from an electrochemical perspective and employed in the construction of three-dimensional pillared networks, thereby providing a synthetic strategy for the development of new solid-state materials, supported by a comprehensive range of characterisation techniques. Both ligands are appended with benzyl groups and display redox-active cores: pteridine-dione for **L1** (pyrimidine-2,4-dione, 6 membered ring) and imidazopyrazinone for **L2** (imidazolidin-2-one, 5 membered ring), which is thus a symmetrical core. In CH_2Cl_2 solution, both **L1** and **L2** exhibit reversible reduction processes, occurring at lower potentials for **L1**. DFT calculations confirm the observed electrochemical trends, and spectroelectrochemical studies involving EPR, evidenced, in both cases, the formation of the radical anions and the density of spins on the different rings. This is the first study evidencing the electrochemical properties of imidazolonequinoxaline derivatives.

The coordination abilities of both pillars **L1** and **L2** were investigated and it was revealed that in the presence of a metal and a dicarboxylic acid, interpenetrated 3D pillared MOFs are formed, that are named **L1-M** (M = Co, Ni, Cu and Zn) and **L2-M** (M = Co, Ni and Zn). The electrochemical ability of **L2-Zn** and **L2-Co** was checked using solid-state electrochemistry, and a reduction process was found centered on the ligands.

This comparative study provides new insight into the electrochemical behavior of the two parent species and their ability to coordinate to transition metals. These investigations demonstrate the feasibility of developing new, robust redox-active ligands that can be incorporated into molecular networks. This provides new perspectives for the development of new materials for energy storage applications, for example.

Author contributions

Jaison Casas: formal analysis, investigation and methodology; Shaban Raja Muhammad: formal analysis and investigation; David Pianca: formal analysis, investigation and methodology; Nolwenn Le Breton: investigation and data curation; Sylvie Choua: investigation, data curation, writing, reviewing and supervision; Nathalie Kyritsakas: investigation and data curation; Christophe Gourlaouen: investigation and data curation; Abdelaziz Jouaiti: methodology, reviewing and supervision; Sylvie Ferlay: methodology, funding, writing, reviewing, editing and supervision.

All authors have given approval to the final version of the manuscript.

Conflicts of interest

There are no conflicts to declare.

Data availability

The data supporting this article have been included as part of the supplementary information (SI). Supplementary information: UV characterization of **L1** and **L2** in solution, proposed redox-behaviour from electrochemical studies in the solid state, the numbering scheme for **L1** and **L2**, DFT calculations for **L1** and **L2**, representation of **L2-Zn** from the crystallographic data, crystallographic data, selected bond lengths, representation and description of **L1-Co** from preliminarily crystallographic data, PXRD patterns and TGA traces for **L2-M** (M = Zn, Ni and Co) and **L1-M** (M = Zn, Ni, Co and Cu) and N_2 adsorption for **L1-M** (M = Co and Zn). See DOI: **https://doi.org/10.1039/d5qi02572a**.

CCDC 2515971 (**L2-Zn**) contains the supplementary crystallographic data for this paper.[62]

Acknowledgements

Financial support from the University of Strasbourg, Unistra, and the CNRS (INC) is acknowledged. For the XRD resolution of the structures, the Service de radiocristallographie de la Fédération de Chimie Le Bel – UAR 2042 is warmly acknowledged. We thank the Agence Nationale de la Recherche (ANR) through the BattAllox Project ANR-20-CE05-0005. Sidonie Brillard is warmly acknowledged for performing some CV measurements. The French research infrastructure INFRANALYTICS FR2054 is acknowledged for its support.

References

1 J. Su, S. Yuan, H. Y. Wang, L. Huang, J. Y. Ge, E. Joseph, J. Qin, T. Cagin, J. L. Zuo and H. C. Zhou, Redox-switchable breathing behavior in tetrathiafulvalene-based metal-organic frameworks, *Nat. Commun.*, 2017, **8**, 2008, DOI: **10.1038/s41467-017-02256-y**.

2 D. M. D'Alessandro, Exploiting redox activity in metal-organic frameworks: concepts, trends and perspectives, *Chem. Commun.*, 2016, **52**, 8957–8971, DOI: **10.1039/C6CC00805D**.

3 J. J. Calbo, M. J. Golomb and A. Walsh, Redox-active metal-organic frameworks for energy conversion and storage, *J. Mater. Chem. A*, 2019, **7**, 16571–16579, DOI: **10.1039/C9TA04680A**.

4 H. C. Zhou, J. R. Long and O. M. Yaghi, *Chem. Rev.*, 2012, **112**, DOI: **10.1021/cr300014x**. Metal-organic frameworks special issue.

5 H.-C. Zhou and S. Kitagawa, Metal-Organic Frameworks (MOFs), *Chem. Soc. Rev.*, 2014, **43**, 5415–5418, DOI: **10.1039/C4CS90059F**.

6 M. Dincă and J. R. Long, Porous framework chemistry special issue, *Chem. Rev.*, 2020, **120**, 673–674, DOI: **10.1021/acs.chemrev.0c00836**.

7 S. A. A. Razavi, W. Chen, H.-C. Zhou and A. Morsali, Tuning redox activity in Metal-Organic Frameworks: from structure to application, *Coord. Chem. Rev.*, 2024, **517**, 216004, DOI: **10.1016/j.ccr.2024.216004**.

8 B. Ding, M. B. Solomon, C. F. Leong and D. M. D'Alessandro, Redox-active ligands: recent advances towards their incorporation into coordination polymers and metal–organic frameworks, *Coord. Chem. Rev.*, 2021, **439**, 213891, DOI: **10.1016/j.ccr.2021.213891**.

9 M. Souto, K. Strutynski, M. Melle-Franco and J. Rocha, Electroactive organic building blocks for the chemical design of functional porous frameworks (MOFs and COFs) in electronics, *Chem. – Eur. J.*, 2020, **26**, 10912–10935, DOI: **10.1002/chem.202001211**.

10 Y.-G. Weng, Z.-H. Ren, Z.-R. Zhang, J. Shao and Q.-Y. Zhu, Tetrathiafulvalene-cobalt metal–organic frameworks for lithium-ion batteries with superb rate capability, *Inorg. Chem.*, 2021, **60**, 17074–17082, DOI: **10.1021/acs.inorgchem.1c02304**.

11 F. Solano, P. Auban-Senzier, I. Olejniczak, B. Barszcz, T. Runka, P. Alemany, E. Canadell, N. Avarvari and N. Zigon, Bis(vinylenedithio)-tetrathiafulvalene-based coordination networks, *Chem. – Eur. J.*, 2023, **29**, e202203138, DOI: **10.1002/chem.202203138**.

12 L. Zhao, W. Cai, G. Ji, J. Wei, Z. Du, C. He and C. Duan, Anthraquinone-based metal-organic frameworks as a bifunctional photocatalyst for C–H activation, *Inorg. Chem.*, 2022, **61**, 9493–9503, DOI: **10.1021/acs.inorgchem.2c00441**.

13 Y. Y. Grisan Qiu, S. Mearini, D. Baranowski, I. Cojocariu, M. Jugovac, G. Zamborlini, P. Gargiani, M. Valvidares, V. Feyer and C. M. Schneider, Robust high-spin Fe^{2+} centers in 2D TCNQ-based metal–organic frameworks, *Inorg. Chem. Front.*, 2025, **12**, 2334–2340, DOI: **10.1039/D4QI03123G**.

14 L. S. Xie, G. Skorupskii and M. Dincă, Electrically conductive metal–organic frameworks, *Chem. Rev.*, 2020, **120**, 8536–8580, DOI: **10.1021/acs.chemrev.9b00766**.

15 J. Wang, H. Wei, J. Guan, K. Müllen and M. Yin, Perylene- and, Perylene Diimide-based Framework Materials Constructed through Metal Coordination, *Chem. – Eur. J.*, 2025, **31**, e202403234, DOI: **10.1002/chem.202403234**.

16 N. Contreras-Pereda, S. Pané, J. Puigmartí-Luis and D. Ruiz-Molina, Conductive properties of triphenylene MOFs and COFs, *Coord. Chem. Rev.*, 2022, **460**, 214459, DOI: **10.1016/j.ccr.2022.214459**.

17 W.-Q. Kan, S.-Z. Wen, Y.-C. He and C.-Y. Xu, Viologen-Based Photochromic Coordination Polymers for Inkless

and Erasable Prints, *Inorg. Chem.*, 2017, **56**, 14926–14935, DOI: 10.1021/acs.inorgchem.7b02206.

18 S. Wang, L. Zhao, H. Sun, Y. Wu, R. Wang, S. Zhang, L. Du and Q.-H. Zhao, Two novel three-dimensional tetraphenylethylene-based rare earth MOFs with ultra-high proton conductivity and performance stability, *Chem. – Eur. J.*, 2022, **28**, e202202154, DOI: 10.1002/chem.202202154.

19 S. R. Ahrenholtz, C. C. Epley and A. J. Morris, Solvothermal preparation of an electrocatalytic metalloporphyrin MOF thin film and its redox hopping charge-transfer mechanism, *J. Am. Chem. Soc.*, 2014, **136**, 2464–2472, DOI: 10.1021/ja410684q.

20 D. Micheroni, G. Lan and W. Lin, Efficient electrocatalytic proton reduction with carbon nanotube-supported metal–organic frameworks, *J. Am. Chem. Soc.*, 2018, **140**, 15591–15595, DOI: 10.1021/jacs.8b09521.

21 L. Li, R. Matsuda, I. Tanaka, H. Sato, P. Kanoo, H. J. Jeon, M. L. Foo, A. Wakamiya, Y. Murata and S. Kitagawa, A crystalline porous coordination polymer decorated with nitroxyl radicals catalyzes aerobic oxidation of alcohols, *J. Am. Chem. Soc.*, 2014, **136**, 7543–7546, DOI: 10.1021/ja5019095.

22 G. Valente, P. Ferreira, M. A. Hernández-Rodríguez, C. D. S. Brites, J. S. Amaral, P. Zelenovskii, F. A. Almeida Paz, S. Guieu, J. Rocha and M. Souto, Exploring the luminescence, redox, and magnetic properties in a multivariate metal–organic radical framework, *Chem. Mater.*, 2024, **36**, 1333–1341, DOI: 10.1021/acs.chemmater.3c02460.

23 D. D. Maspoch, D. Ruiz-Molina, K. Wurst, N. Domingo, M. Cavallini, F. Biscarini, J. Tejada, C. Rovira and J. Veciana, A nanoporous molecular magnet with reversible solvent-induced mechanical and magnetic properties, *Nat. Mater.*, 2003, **2**, 190–195, DOI: 10.1038/nmat834.

24 C. Walsh, Naturally occurring 5-deazaflavin coenzymes: biological redox roles, *Acc. Chem. Res.*, 1986, **19**, 216–221, DOI: 10.1021/ar00127a004.

25 J. Hong, M. Lee, B. Lee, D.-H. Seo, C. B. Park and K. Kang, Biologically inspired pteridine redox centres for rechargeable batteries, *Nat. Commun.*, 2014, **5**, 5335, DOI: 10.1038/ncomms6335.

26 K. Lin, R. Gomez-Bombarelli, E. S. Beh, L. Tong, Q. Chen, A. Valle, A. Aspuru-Guzik, M. J. Aziz and R. G. Gordon, A redox-flow battery with an alloxazine-based organic electrolyte, *Nat. Energy*, 2016, **1**, 16102, DOI: 10.1038/nenergy.2016.102.

27 J. Casas, D. Pianca, N. L. Breton, A. Jouaiti, C. Gourlaouen, M. Desage-El Murr, S. Le Vot, S. Choua and S. Ferlay, Alloxazine-based ligands appended with coordinating groups: synthesis, electrochemical studies, and formation of coordination polymers, *Inorg. Chem.*, 2024, **63**, 4802–4806, DOI: 10.1021/acs.inorgchem.3c04550.

28 J. Casas, A. I. Vicatos, L. J. Barbour, N. Kyritsakas, A. Jouaiti and S. Ferlay, Series of microporous redox-active pillared MOFs based on alloxazine ligands, *ChemistryOpen*, 2025, e202500461, DOI: 10.1002/open.202500461.

29 J. Casas, A. I. Vicatos, N. Kyritsakas, S. Le Vot, A. Jouaiti and S. Ferlay, Rational formation of porous pillared alloxazine based MOFs: pore opening effect and redox properties, 2025, submitted.

30 V. Guillerm, D. Kim, J. F. Eubank, R. Luebke, X. Liu, K. Adil, M. S. Lah and M. Eddaoudi, A supermolecular building approach for the design and construction of metal-organic frameworks, *Chem. Soc. Rev.*, 2014, **43**, 6141–6172, DOI: 10.1039/C4CS00135D.

31 F. Zarekarizi, M. Joharian and A. Morsali, Pillar-layered MOFs: functionality, interpenetration, flexibility and applications, *J. Mater. Chem. A*, 2018, **6**, 19288–19329, DOI: 10.1039/C8TA03306D.

32 J. J. M. Cameron, C. Holc, A. J. Kibler, C. L. Peake, D. A. Walsh, G. N. Newton and L. R. Johnson, Molecular redox species for next-generation batteries, *Chem. Soc. Rev.*, 2021, **50**, 5863–5883, DOI: 10.1039/D0CS01507E.

33 V. E. Semenov, R. K. Giniyatullin, D. R. Sharafutdinova and V. S. Reznik, *Russ. J. Org. Chem.*, 2010, **46**, 439–443, DOI: 10.1134/S1070428010030243.

34 F. Yoneda, M. Noguchi, M. Noda and Y. Nitta, Synthesis of imidazo[4,5-e]-as-triazine (6-azapurine) derivatives, *Chem. Pharm. Bull.*, 1978, **26**, 3154–3160, DOI: 10.1248/cpb.26.3154.

35 S. B. Smith and T. C. Bruice, Mechanisms of isoalloxazine (flavine) hydrolysis, *J. Am. Chem. Soc.*, 1975, **97**, 2875–2881, DOI: 10.1021/ja00843a043.

36 H. I. X. Mager, Activation and transfer of oxygen-XII: alkoxy adducts derived from I,3,10-trimethylalloxazinium (1,3-dimethylflavinium) cations, *Tetrahedron*, 1977, **33**, 981–989, DOI: 10.1016/0040-4020(77)80212-3.

37 T. Harayama, Y. Tezuka, T. Taga and F. Yoneda, Hydrolysis products of flavins (isoalloxazines), *J. Chem. Soc., Perkin Trans. 1*, 1987, 75–83, DOI: 10.1039/P19870000075.

38 V. E. Semenov, R. K. Giniyatullin, D. R. Sharafutdinova and V. S. Rezni, Ring Contraction of 1,3-Bis(5-bromopentyl) alloxazine, *Russ. J. Org. Chem.*, 2010, **46**, 439–443, DOI: 10.1134/S1070428010030243.

39 A. Rehpenn, S. Hindelang, K.-N. Truong, A. Pöthig and G. Storch, Enhancing flavins photochemical activity in hydrogen atom abstraction and triplet sensitization through ring-contraction, *Angew. Chem., Int. Ed.*, 2024, **63**, e202318590, DOI: 10.1002/anie.202318590.

40 S. Iwata and K. Tanaka, Electrochemical properties of pyrido[1′,2′:1,2]imidazo[4,5-b]pyrazine and pyrido[1′,2′:1,2]imidazo[4,5-b]quinoxaline derivatives, *J. Heterocycl. Chem.*, 1998, **35**, 939–941, DOI: 10.1002/jhet.5570350426.

41 M. J. Clarke and M. G. Dowling, Cyclic voltammetry studies of metalloflavin complexes in aqueous solution, *Inorg. Chem.*, 1981, **20**, 3506–3514, DOI: 10.1021/ic50224a070.

42 F. M. Hornung, O. Heilmann, W. Kaim, S. Zalis and J. Fiedler, Metal vs ligand reduction in complexes of 1,3-dimethylalloxazine (DMA) with copper(I), ruthenium(II), and tungsten(VI): crystal structures of (DMA)WO_2Cl_2 and (Bis(1-methylimidazol-2-yl)ketone)WO2Cl2, *Inorg. Chem.*, 2000, **39**, 4052–4058, DOI: 10.1021/ic0001816.

43 J. R. Ames, M. A. Houghtaling and D. L. Terrian, Cyclic voltammetry of some quinoxaline di-N-oxides and quinoxa-

lines in dimethylformamide, *Electrochim. Acta*, 1992, **37**, 1433–1436, DOI: 10.1016/0013-4686(92)87018-U.

44 M. Maruyama and K. Murakami, Electrochemical behavior of nitrogen heterocycles in N,N-dimethylformamide-water and aqueous buffer solution, *J. Electroanal. Chem.*, 1979, **102**, 221–235, DOI: 10.1016/S0022-0728(79)80393-9.

45 *Flavins: Photochemistry and Photobiology*, ed. E. Silva and A. M. Edwards, RSC Publishing, 2006.

46 W. Kaim, B. Schwederski, O. Heilmann and F. M. Hornung, Coordination compounds of pteridine, alloxazine and flavin ligands: structures and properties, *Coord. Chem. Rev.*, 1999, **182**, 323–342, DOI: 10.1016/S0010-8545(98)00193-3.

47 A. Das, H. Jobelius, J. Schleinitz, S. Gamboa-Ramirez, G. Creste, G. Kervern, J. Raya, N. L. Breton, A. Guénet, Z. Boubegtiten-Fezoua, L. Grimaud, M. Orio, G. Rogez, P. Hellwig, S. Choua, S. Ferlay and M. Desage-El Murr, A hybrid bioinspired catechol-alloxazine triangular nickel complex stabilizing protons and electrons, *Inorg. Chem. Front.*, 2021, **8**, 5286–5298, DOI: 10.1039/D1QI01131F.

48 A. L. Spek, Single-crystal structure validation with the program PLATON, *J. Appl. Crystallogr.*, 2003, **36**, 7–13, DOI: 10.1107/S0021889802022112.

49 E. P. Barrett, L. G. Joyner and P. P. Halenda, The Determination of Pore Volume and Area Distributions in Porous Substances. I. Computations from Nitrogen Isotherms, *J. Am. Chem. Soc.*, 1951, **73**, 373–380, DOI: 10.1021/ja01145a126.

50 S. Stoll and A. J. Schweiger, EasySpin, a comprehensive software package for spectral simulation and analysis in EPR, *Magn. Reson.*, 2006, **178**, 42–55, DOI: 10.1016/j.jmr.2005.08.013.

51 G. te Velde, F. M. Bickelhaupt, E. J. Baerends, C. F. Guerra, S. J. A. van Gisbergen, J. G. Snijders and T. Ziegler, Chemistry with ADF, *J. Comput. Chem.*, 2001, **22**, 931–967, DOI: 10.1002/jcc.1056.

52 P. J. Stephens, F. J. Devlin, C. F. Chabalowski and M. J. Frisch, Ab initio calculation of vibrational absorption and circular dichroism spectra using density functional force fields, *J. Phys. Chem.*, 1994, **98**, 11623–11627, DOI: 10.1021/j100096a001.

53 S. Grimme, J. Anthony, S. Ehrlich and H. Krieg, A consistent and accurate ab initio parametrization of density functional dispersion correction (DFT-D) for the 94 elements H–Pu, *J. Chem. Phys.*, 2010, **132**, 154104, DOI: 10.1063/1.3382344.

54 C. Lee, W. Yang and R. G. Parr, Development of the Colle-Salvetti correlation-energy formula into a functional of the electron density, *Phys. Rev. B:Condens. Matter Mater. Phys.*, 1988, **37**, 785–789, DOI: 10.1103/physrevb.37.785.

55 A. D. Becke, Density-functional thermochemistry. III. The role of exact exchange, *J. Chem. Phys.*, 1993, **98**, 5648–5652, DOI: 10.1063/1.464913.

56 C. Pye and T. Ziegler, An implementation of the conductor-like screening model of solvation within the Amsterdam density functional package, *Theor. Chem. Acc.*, 1999, **101**, 396–408, DOI: 10.1007/s002140050457.

57 F. Neese, *ORCA: An ab initio, DFT and semiempirical electronic structure package, version 2.9.1*, Universität Bonn, Bonn, Germany, 2012.

58 F. Neese, Calculation of the zero-field splitting tensor on the basis of hybrid density functional and Hartree-Fock theory, *J. Chem. Phys.*, 2007, **127**, 164112, DOI: 10.1063/1.2772857.

59 *M86-EXX229V1 APEX3 User Manual*, Bruker AXS Inc., Madison, USA, 2016.

60 G. M. Sheldrick, SHELXT – Integrated space-group and crystal-structure determination, *Acta Crystallogr., Sect. A: Found. Adv.*, 2015, **71**, 3–8, DOI: 10.1107/S2053273314026370.

61 G. M. Sheldrick, Crystal structure refinement with SHELXL, *Acta Crystallogr., Sect. C: Struct. Chem.*, 2015, **71**, 3–8, DOI: 10.1107/S2053229614024218.

62 CCDC 2515971: Experimental Crystal Structure Determination, 2026, DOI: 10.5517/ccdc.csd.cc2qg2cn.

